Neutron activation of natural zinc samples at $kT = 25$ keV

R. Reifarth,[1] S. Dababneh,[2] M. Heil,[3] F. Käppeler,[4] R. Plag,[1] K. Sonnabend,[1] and E. Uberseder[5]
[1]*Goethe Universität Frankfurt, 60438 Frankfurt am Main, Germany*
[2]*Department of Physics, Faculty of Science, Al-Balqa Applied University, P.O. Box 2587, Amman 11941, Jordan*
[3]*GSI Helmholtzzentrum für Schwerionenforschung GmbH, 64291 Darmstadt, Germany*
[4]*Karlsruhe Institute of Technology, Campus Nord, Institut für Kernphysik, 76021 Karlsruhe, Germany*
[5]*University of Notre Dame, Department of Physics, Notre Dame, Indiana, USA*
(Received 22 December 2011; revised manuscript received 23 February 2012; published 12 March 2012)

The neutron-capture cross sections of ^{64}Zn, ^{68}Zn, and ^{70}Zn have been measured with the activation technique in a quasistellar neutron spectrum corresponding to a thermal energy of $kT = 25$ keV. By a series of repeated irradiations with different experimental conditions, an uncertainty of 3% could be achieved for the ^{64}Zn$(n,\gamma)^{65}$Zn cross section and for the partial cross section ^{68}Zn$(n,\gamma)^{69}$Zn^m feeding the isomeric state in ^{69}Zn. For the partial cross sections ^{70}Zn$(n,\gamma)^{71}$Zn^m and ^{70}Zn$(n,\gamma)^{71}$Zn^g, which had not been measured so far, uncertainties of only 16% and 6% could be reached because of limited counting statistics and decay intensities. Compared to previous measurements on ^{64,68}Zn, the uncertainties could be significantly improved, while the ^{70}Zn cross section was found to be two times smaller than existing model calculations. From these results Maxwellian average cross sections were determined between 5 and 100 keV. Additionally, the β-decay half-life of ^{71}Zn^m could be determined with significantly improved accuracy. The consequences of these data have been studied by network calculations for convective core He burning and convective shell C burning in massive stars.

DOI: 10.1103/PhysRevC.85.035802 PACS number(s): 25.40.Lw, 26.20.Kn, 27.40.+z, 27.50.+e

I. INTRODUCTION

The signature of the s-process contribution to the solar abundances implies two parts: a *main* component, which is responsible for the mass region from Y to Bi, and a *weak* component, which dominates in the region between Fe and Sr. The main component can be assigned to low-mass stars with $1 \leqslant M/M_\odot \leqslant 3$, whereas the weak component is related to massive stars with $M \geqslant 8M_\odot$ ($M_\odot$ stands for the mass of the sun). Because of the much shorter evolution times of massive stars, the s-process enrichment of the Universe starts with the lighter s elements. Accordingly, the weak s process is important for the early stellar populations and for galactic chemical evolution in general [1,2].

The s process in massive stars occurs in two steps during different evolutionary phases. Neutrons are mainly produced by the ^{22}Ne$(\alpha,n)^{25}$Mg reaction in both cases, but at rather different temperatures and neutron densities. During core He burning, neutrons are produced near core He exhaustion at temperatures of $T = (2.5\text{–}3.5) \times 10^8$ K for about 10^4 years with neutron densities $\lesssim 10^6$ cm^{-3}, whereas the higher temperatures of $T = (1.0\text{–}1.4) \times 10^9$ K during the subsequent carbon-shell burning phase give rise to peak neutron densities of about 10^{12} cm^{-3} [3–5].

In the scenarios for the main and weak s processes, the stellar (n,γ) cross sections of the involved isotopes constitute the essential nuclear physics input, but with an important difference: The high neutron exposure during the main component leads to equilibrium in the reaction flow, expressed by the so-called local approximation $\langle\sigma\rangle N_s =$ constant, which holds true for isotopes between magic neutron numbers. This relation implies that the emerging s abundances are inversely proportional to the stellar cross sections and that the uncertainty of a particular cross section affects only the abundance of that specific isotope. In contrast, the neutron exposure in massive stars is too small to achieve flow equilibrium, and this means that cross section uncertainties are not only influencing the abundance of that particular isotope but have a potentially strong propagating effect on the abundances of the subsequent isotopes involved in the s-process chain.

This propagation effect was first discussed for the ^{62}Ni$(n,\gamma)^{63}$Ni reaction [6] and later investigated for the complete reaction chain of the weak s process [7–9]. Computations with different choices for the Maxwellian averaged cross sections (MACS) showed important bottle-neck effects and the significant impact of crucial capture rates near the Fe seed on the abundances of the subsequent isotopes in the reaction chain. Limitations in the quality of stellar cross sections can, therefore, have serious consequences for the contributions of the weak s process to galactic chemical evolution.

Stellar neutron-capture cross sections in the mass region of the weak s process are often not available with the required accuracy. In case of the Zn isotopes, experimental data suffer from large uncertainties or are even missing, as for ^{70}Zn [10,11]. Therefore, a series of activation measurements has been performed at the Karlsruhe 3.7 MV Van de Graaff accelerator on natural Zn to improve the accessible cross sections for ^{64,70}Zn and for the partial cross section of ^{68}Zn. Because these isotopes have relatively small cross sections of less than about 50 mb, they are expected to give rise to large propagation effects in the final abundance distribution.

Apart from its propagation effect in the weak s process, Zn is of general interest for galactic evolution. Though it is commonly accepted that Zn is produced by a variety of scenarios, the respective nucleosynthesis mechanisms and their relative contributions are poorly understood. Spectroscopic

 ©2012 American Physical Society

observations over a range of stellar metallicities (e.g., Refs. [12–14]) found indications of an overabundance of Zn compared to Fe in low-Z stars, but an explanation for this excess appears premature in view of the present uncertainties concerning the origin of Zn. In massive stars, the s-process component of the Zn isotopes is obscured by the fact that measured neutron-capture cross sections are scarce, uncertain, or even missing.

Experimental technique and measurements are described in Sec. II, and Secs. III and IV deal with data analysis and results. Maxwellian average cross sections (MACS) and the related astrophysical aspects are discussed in Sec. V.

II. MEASUREMENTS

A. Experimental technique

The activation method represents a well established and accurate approach to determine MACS at $kT = 25$ keV by producing a quasistellar neutron spectrum via the ^{7}Li$(p,n)^7$Be reaction [15]. This method has been extensively used, mostly for measurements related to the main s-process component (for examples see Refs. [16–18]). In the present experiment, a proton beam with an energy of $E_p = 1912$ keV, 30 keV above the reaction threshold, was delivered by the Karlsruhe 3.7 MV Van de Graaff accelerator with typical intensities of 100 μA. The neutron production targets consisted of 30 μm thick metallic Li layers evaporated onto water-cooled copper backings. In this way, neutrons are kinematically collimated into a forward cone of 120° opening angle. Neutron moderation is avoided since cooling is achieved by lateral heat conduction to the water flow outside of this cone. Throughout the irradiations the neutron flux was continuously monitored and recorded in time steps of typically 60 s by means of a ^{6}Li-glass detector at 1 m distance from the target. This information is important to account for fluctuations of the neutron yield in evaluating the fraction of the reaction products that decay already during the irradiations.

For a sketch of the experimental setup and more details see Ref. [7], for example.

B. Samples and irradiations

In total, four activations were performed with three metallic Zn samples 8 and 12 mm in diameter and 0.5 and 1 mm in thickness to minimize uncertainties stemming from sample geometry (Table I). The samples were sandwiched between 0.03 mm thick gold foils of the same diameter, which served as neutron flux monitors using the well known Au reference cross section [19]. During the activations the samples were placed completely inside the neutron cone in contact with the neutron target at the position of highest flux. The relative isotope abundance ratios adopted from Ref. [20] are 48.268(214) for ^{64}Zn, 19.024(82) for ^{68}Zn, and 0.631(6) for ^{70}Zn.

Activation times were chosen between 3 and 44 h according to the half-lives of the various product nuclei and to test the respective time-dependent corrections applied in data analysis. The integrated flux values listed in Table I correspond to average fluxes between 0.6 and 1.1×10^9 s^{-1}, depending on the performance of the accelerator and of the Li target.

TABLE I. Zn samples and irradiation parameters.

Activation	Sample	Mass (mg)	Diameter (mm)	Irradiation time (min)	Integrated flux ($\times 10^{13}$)
I	Zn-1	409.19	12	174	1.12(4)
II	Zn-1	409.19	12	2640	14.2(5)
III	Zn-2	181.71	8	1182	7.4(3)
IV	Zn-3	800.72	12	1242	4.9(3)

C. Induced activities

The induced activities are characterized by energetic γ-ray lines. The corresponding decay data are listed in Table II. The higher activities of the gold foils were measured with a well calibrated, passively shielded 76 cm^3 HPGe detector, with 1.7 keV resolution at 1.33 MeV γ-ray energy and a relative efficiency of 30%.

The Zn activities were counted with two clover-type HPGe detectors facing each other in close geometry. Each clover detector (Eurisys Measures) consists of four independent n-type Ge crystals in a four-leaf-clover arrangement with 0.2 mm gaps in between. The originally cylindrical crystals 50 mm in diameter and 70 mm in length are shaped as shown in Fig. 1, leaving an active volume of about 145 cm^3 per crystal. The crystals are held from the rear through a steel rod 1 mm in diameter and about 35 mm in length and are enclosed in a common cryostat. The front end of the crystals is separated by a gap of 5 mm from the 1 mm thick aluminum window.

The individual Ge crystals have a resolution of typically 2.0 keV at 1.33 MeV. At 122 keV, the peak-to-total ratio is ~45. The detector can be operated either in single mode by considering the signals from each crystal independently, or in calorimetric mode when coincident signals from different crystals are added off-line. In this way Compton-scattered events can be restored in the sum spectrum if the scattered photon is detected in one of the neighboring crystals, resulting in a significantly higher full-energy-peak efficiency.

In both setups, the counting position could be reproduced within 0.1 mm by means of special adapters. This feature was crucial for obtaining a well defined efficiency, especially for the close geometry of the two clover detectors.

Examples for the accumulated γ spectra are shown in Fig. 2 for the 1115 keV line in the decay of ^{65}Zn, for the 487 keV line from ^{71}Zn^{m}, and for the 910 keV line from ^{71}Zn^{g}.

The efficiency of the clover setup was determined with a set of pointlike calibration sources (^{22}Na, ^{54}Mn, ^{60}Co, ^{65}Zn, ^{88}Y, ^{131}Ba, and ^{137}Cs) complemented by a detailed Monte Carlo

TABLE II. Decay properties of the product nuclei.

Product nucleus	Half-life	γ-ray energy (keV)	Intensity per decay (%)	Ref.
^{65}Zn	243.93(9) d	1115.539(2)	50.04(10)	[21]
^{69}Zn^{m}	13.76(2) h	438.636(18)	94.8(2)	[22]
^{71}Zn^{g}	2.45(10) min	910.3(1)	7.84(64)	[23]
^{71}Zn^{m}	3.96(5) h	487.30(4)	61.2(23)	[23]
^{198}Au	2.69517 (21) d	411.80205(17)	95.62(6)	[24]

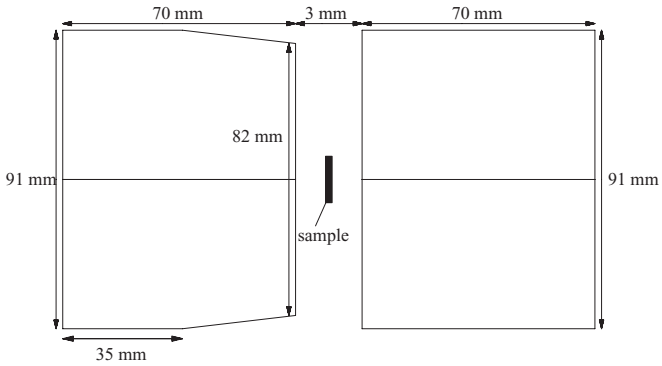

FIG. 1. Schematic view of the HPGe spectrometer consisting of two clover-type detectors in close geometry.

simulation using a full model of the setup as sketched above. These simulations were particularly important for determining the efficiencies in the calorimetric mode, which was used for the 910 keV transition in the decay of ^{71}Zn^{g}. The absolute efficiencies for the two detection modes of the clover setup are compared in Fig. 3. A detailed description of the simulations and the calibration procedure is given in Ref. [25].

The simulations provided also the small corrections to the measured peak detection efficiency values for the pointlike calibration sources (ϵ_γ). These corrections, which are listed in Table III, refer to the actual diameter of the samples ($K_{\rm ext}$), to γ-ray absorption in the sample ($K_{\rm abs}$), and to the possible summing of cascade transitions ($K_{\rm sum}$).

III. DATA ANALYSIS

A. Half-life of ^{71}Zn^{m}

The induced activities were followed in time steps of 30 min to exclude parasitic activities, which might have contributed to the characteristic γ lines listed in Table II. The time sequence obtained for ^{71}Zn^{m} showed a significant deviation from the expected half-life of $t_{1/2}^{\rm rec} = 3.96(5)$ h [23]. This value represents a weighted average of measurements that were performed about 50 years ago using different techniques to produce ^{71}Zn^{m} and observe its decay [26–28] (see Table IV).

The decay curves based on the γ transitions with energies of 386, 487, and 620 keV in ^{71}Ga are shown in Fig. 4 for about seven half-lives of ^{71}Zn^{m}. The activity was followed for more than ten half-lives until no significant signals above background could be detected. The weighted average derived from a fit to these decay curves results in new half-life of 4.125(7) h, with a significantly improved uncertainty compared to the previously determined value [23].

Combining this new result with the former values as listed in Table IV yields a weighted average of 4.120(7) h. Only with this revised half-life does the deduced cross section for the reaction ^{71}Zn^{m} become independent of the time interval chosen for the activity determination. This was impossible to achieve using the previously determined half-life [23].

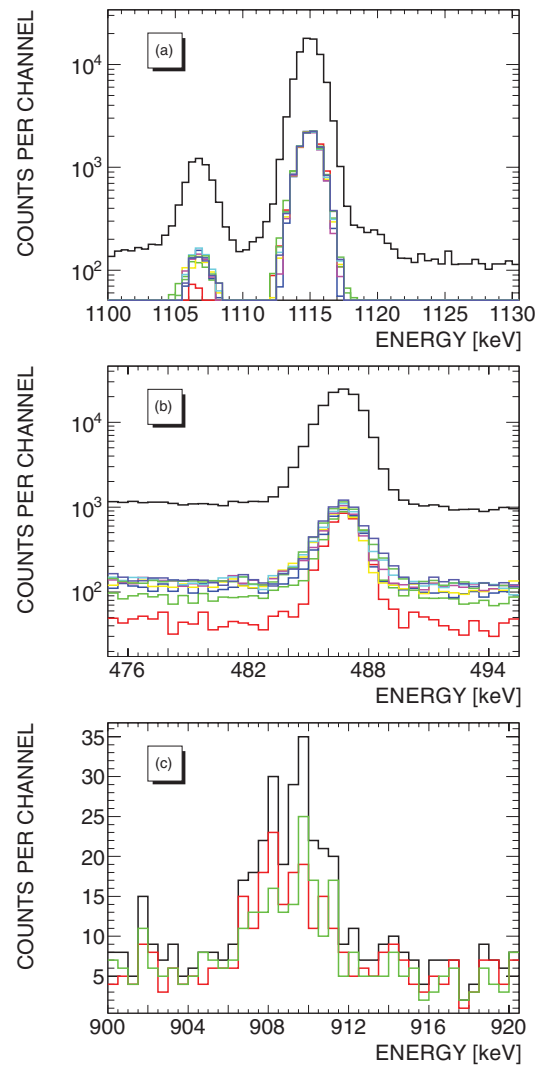

FIG. 2. (Color online) Examples for the γ-ray spectra measured after the irradiations. Shown from top to bottom are the decay lines of ^{65}Zn at 1115 keV (a), ^{71}Zn^{m} at 487 keV (b), and the very weak line from ^{71}Zn^{g} at 910 keV (c). The spectra of the eight individual crystals in the HPGe clover detectors are plotted together with the respective sum. The calorimetric mode was used only in case (c) for improving the signal/background ratio.

B. Cross-section determination

The total number of activated nuclei A is given by

$$A = \phi N \sigma f_b, \tag{1}$$

where ϕ is the time-integrated neutron flux, N is the number of sample atoms, and σ is the spectrum-averaged neutron capture cross section. The factor f_b accounts for variations of the neutron flux and for the decay during activation.

The number of activated nuclei in Eq. (1) is determined from the number of counts in a characteristic γ-ray line,

$$C_\gamma = A K_\gamma \varepsilon_\gamma I_\gamma [1 - \exp(-\lambda t_m)] \exp(-\lambda t_w), \tag{2}$$

where K_γ combines the correction factors listed in columns 5–7 of Table III, ε_γ is the efficiency of the HPGe-detection system, I_γ is the line intensity, t_w is the waiting time between

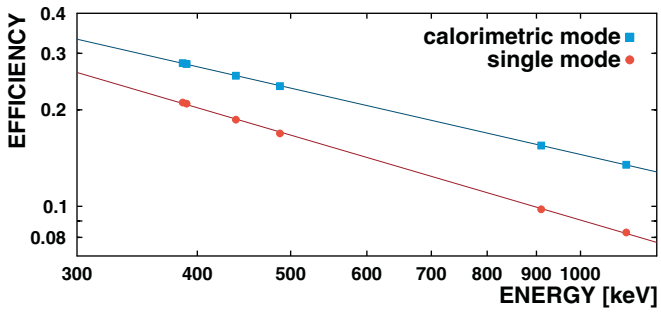

FIG. 3. (Color online) Comparison of the γ-ray efficiency of the clover setup for the two detection modes. The symbols show simulated efficiencies for the γ rays emitted in the decay of ^{65}Zn, ^{69}Zn^{m}, ^{71}Zn^{m}, and ^{71}Zn^{g}, respectively. The lines represent a fit of the function $\varepsilon(E) = aE^b$ to the simulated values. The efficiency in the calorimetric mode is on average a factor of 1.45 greater than that of the single mode.

irradiation and γ-spectroscopy, and t_m is the duration of the activity measurement.

The time-integrated flux at the sample position, ϕ, is determined from the intensities of the 412 keV γ-ray line in the spectra of the gold foils [29],

$$\phi = \frac{\phi_1 + \phi_2}{2} \tag{3}$$

with

$$\Delta\phi = \frac{\phi_1 - \phi_2}{4}. \tag{4}$$

The neutron flux seen by the gold samples follows from the number of ^{198}Au nuclei,

$$\phi = \frac{N_{198}}{N_{197}\,\sigma\, f_b}, \tag{5}$$

where the correction f_b accounts for the fraction of ^{198}Au nuclei that decayed already during the irradiation [15]. The spectrum-integrated ^{197}Au(n,γ) cross section is obtained by folding the corresponding neutron spectra, which were calculated with the code PINO [30] (Fig. 5) with the differential

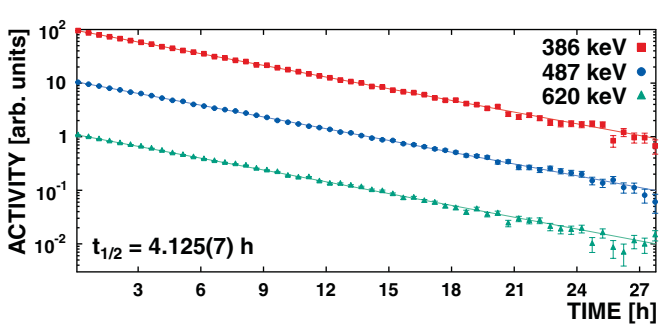

FIG. 4. (Color online) Measured decay curves of ^{71}Zn^{m} for three γ transitions in ^{71}Ga including a fit to the data; see Table IV. The error bars are smaller than the symbols. The given value of $t_{1/2} = 4.125(7)$ h is the weighted average derived from the shown decay curves. It differs significantly from the previously determined half-life of 3.96(5) h [23].

TABLE III. Efficiencies and correction factors compared to ideal pointlike sources for the clover setup in single mode. Only the data for the 910 keV line of ^{71}Zn^{g} are treated in calorimetric mode.

Product nucleus	E_γ (keV)	ϵ_γ	Sample	K_{ext}	K_{abs}	K_{sum}
^{65}Zn	1115	0.0829	Zn-1	0.9894	0.9877	1.0011
			Zn-2	0.9956	0.9836	1.0006
			Zn-3	0.9884	0.9772	0.9978
^{69}Zn^{m}	439	0.1863	Zn-1	0.9901	0.9794	0.999
			Zn-2	0.9938	0.9783	0.9991
			Zn-3	0.9906	0.9592	0.9994
^{71}Zn^{m}	487	0.1688	Zn-1	0.9907	0.9808	0.8577
			Zn-2	0.9949	0.9808	0.8655
			Zn-3	0.9924	0.9606	0.8536
^{71}Zn^{g}	910	0.1547	Zn-1	0.9955	0.9847	0.963

^{197}Au(n,γ) cross section of Macklin [31] normalized to the value for $kT = 25$ keV of Ratynski and Käppeler [19].

The integrated flux values determined by the gold foils and the corresponding average seen by the Zn samples are given in Table V for activation runs I–IV.

C. Uncertainties

The experimental uncertainties are summarized in Table VI, where the investigated reactions are indicated by the respective product nuclei.

Significant contributions to the overall uncertainty originate from the gold reference cross section, the efficiency of the HPGe detectors, and the time-integrated neutron flux. The ^{70}Zn cross sections are also affected by uncertain γ-decay intensities. Any improvement of these data would, therefore, be important.

Because statistical uncertainties were found to be practically negligible after averaging the results from repeated activations, the final uncertainties are determined by systematic effects. Only in case of the partial cross section to the ground state of ^{71}Zn, the counting statistics was not sufficient for achieving an adequate accuracy of the final result.

TABLE IV. Half-life of ^{71}Zn^{m}. The two left columns summarize the values of previous measurements and their weighted average, the value from Ref. [23]. In comparison, the two right columns show the results obtained in this work from the decay curves of three γ transitions in ^{71}Ga and their weighted average (w.a.). The uncertainties correspond to one standard deviation.

Literature values		This work	
Ref.	$t_{1/2}$ (h)	E_γ (keV)	$t_{1/2}$ (h)
[26]	3.92(5)	386	4.142(9)
[27]	4.0(1)	487	4.117(12)
[28]	4.1(1)	620	4.098(15)
w.a. [23]	3.96(5)	w.a.	4.125(7)

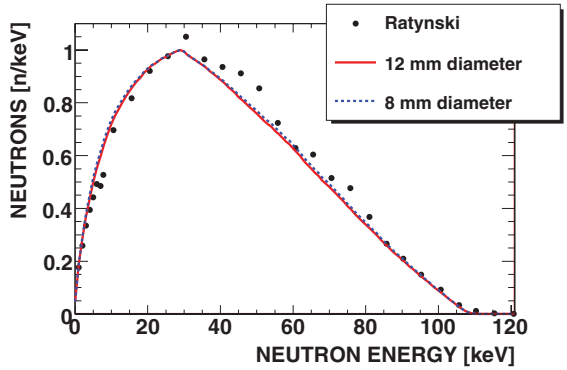

FIG. 5. (Color online) Simulated neutron spectra for the two sample diameters in comparison with the spectrum of Ref. [19]. The simulated spectra contain a weighting factor for neutrons emitted at larger angles with respect to the incoming proton beam, which is not included in the experimental spectrum of Ref. [19]. Details of the simulations can be found in Ref. [30].

IV. RESULTS

A. Measured cross sections

Table VII shows a summary of the results obtained in all four activations together with the corresponding uncertainties. In spite of the variation of the experimental parameters (see Table I), the results are all consistent within the estimated uncertainties, thus confirming the procedures applied in data analysis. These variations included different sample sizes and masses to verify the corrections for finite-size and self-shielding effects, as well as different irradiation times, to control uncertainties due to the half-life of the respective product nucleus.

Previous (n,γ) cross-section data for the investigated isotopes ^{64,68,70}Zn are rather limited [10,32]. For ^{64}Zn as well as for ^{68}Zn, there is only a single measurement based on the time-of-flight (TOF) method. In both cases, uncertainties of 10% have been reported [33,34]. The partial cross section to the isomer in ^{69}Zn has been studied once [35] and was quoted with an uncertainty of 25%, whereas there are no experimental results for ^{70}Zn at all.

As illustrated in Table VII, these uncertainties could be substantially improved. The numerical cross-section data are compared for the MACS values in the following section.

B. Maxwellian averages

The values listed in Table VII represent average cross sections for the experimental neutron distribution used in the irradiations. Though the experimental spectrum corresponds in very good approximation to a thermal spectrum for $kT = 25$ keV, the cutoff at 106 keV requires a small correction, in particular if the investigated cross section exhibits a different energy dependence than the gold reference cross section.

For the calculation of the final MACS,

$$\langle\sigma\rangle_{kT} = \frac{\langle\sigma v\rangle}{v_T} = \frac{2}{\sqrt{\pi}}\frac{\int_0^\infty \sigma(E_n)E_n\exp(-E_n/kT)dE_n}{\int_0^\infty E_n\exp(-E_n/kT)\,dE_n}, \quad (6)$$

the correction was obtained by normalizing the differential (n,γ) cross sections $\sigma_{n,\gamma}(E_n)$, e.g., from theoretical calculations with the Hauser-Feshbach (HF) statistical model [36] or from evaluated data libraries (http://www-nds.iaea.org/), with the new experimental values. Apart from the normalization factor $2/\sqrt{\pi}$ from the definition of the MACS in Eq. (6), these corrections are between 3% and 5%.

TABLE V. Integrated neutron fluxes (in units of 10^{13}) and activation times t_a.

Run	ϕ_1	ϕ_2	ϕ_{sample}	t_a (h)
I	1.20	1.05	1.12 ± 0.04	2.9
II	15.2	13.2	14.2 ± 0.5	44.0
III	7.9	6.8	7.4 ± 0.3	19.7
IV	5.5	4.4	4.9 ± 0.3	20.7

TABLE VI. Compilation of uncertainties. The uncertainties for self-absorption and detector efficiency are the same for all isotopes.

Source of Uncertainty	Uncertainty (%)				
	Au	^{65}Zn	^{69}Zn^{m}	^{71}Zn^{g}	^{71}Zn^{m}
Gold cross section	1.5	—	—	—	—
Number of nuclei	0.1	0.5	0.4	0.9	0.9
Time factors, f_i, $t_{1/2}$		0.1	0.2	4.0	1.3
Self-absorption, K_γ			0.2		
Detector efficiency, ϵ_γ			1.5		
γ-ray intensity, I_γ	0.06	0.2	0.2	8.2	3.8
Time integrated flux, ϕ	—	1.5	1.5	2.5	2.4
Counting statistics		0.7	0.9	13	0.8
Total uncertainty	—	2.8	2.8	16	5.1

TABLE VII. Activations, γ-spectroscopy, and cross-section results. Cross sections are averaged over the quasistellar spectrum.

Activation	γ-ray energy (keV)	Cross section (mb)	Mean value (mb)
	^{64}Zn$(n,\gamma)^{65}$Zn		
I	1115.5	54.5 ± 2.1	
II	1115.5	54.7 ± 2.2	
III	1115.5	52.7 ± 2.2	
IV	1115.5	52.6 ± 3.0	53.5 ± 1.5
	^{68}Zn$(n,\gamma)^{69}$Zn^{m}		
I	438.64	3.27 ± 0.13	
II	438.64	3.38 ± 0.14	
III	438.64	3.25 ± 0.14	
IV	438.64	3.31 ± 0.19	3.30 ± 0.09
	^{70}Zn$(n,\gamma)^{71}$Zn^{g}		
I	910.27	4.18 ± 0.67	4.18 ± 0.67
	^{70}Zn$(n,\gamma)^{71}$Zn^{m}		
I	487.38	6.69 ± 0.40	
II	487.38	7.46 ± 0.43	
III	487.38	6.39 ± 0.37	
IV	487.38	6.75 ± 0.47	6.79 ± 0.34

TABLE VIII. MACS of ^{64}Zn and ^{70}Zn compared to the compilation of Bao *et al.* [10].[a] Since only the partial cross section of ^{68}Zn$(n,\gamma)^{69}$Zn^{m} was measured here, only the total MACS of ^{68}Zn from Ref. [10] are given.

kT (keV)	MACS (mb)										
	5	10	15	20	25	30	40	50	60	80	100
					^{64}Zn$(n,\gamma)^{65}$Zn						
Ref. [10]	139	108	88	75	66	59 ± 5	52	47	44	40	38
Ref. [10][a]	123	95.9	78.2	66.6	58.6 ± 1.7	52.4 ± 1.7	46.2	41.7	39.1	35.5	33.7
					^{68}Zn$(n,\gamma)^{69}$Zn						
Ref. [10]	331	238	197	174	153	139 ± 6	121	113	102	87	79
					^{70}Zn$(n,\gamma)^{71}$Zn						
Ref. [10]	57	38	30	26.3	23.5	21.5 ± 2	18.7	16.9	15.5	13.7	12.5
Ref. [10][b]	28.4	18.9	14.9	13.1	11.7 ± 0.8	10.7 ± 0.8	9.3	8.4	7.7	6.8	6.2

[a]For comparison with measured cross section values in Table VII multiply with $\sqrt{\pi}/2$.
[b]Normalized to the measured value.

The normalized energy-dependent cross sections can also be used for extrapolation to other temperatures as shown in Table VIII. The data from the compilation of Refs. [10,37] are listed before and after normalization to the present results for $kT = 25$ keV

MACS values are commonly compared at the standard thermal energy of $kT = 30$ keV (Table VIII). The value for ^{64}Zn is about 12% lower than the MACS based on previous TOF data [33], but the uncertainty could be reduced by a factor of 2.5. In case of ^{70}Zn, the sum of the partial cross sections is considerably smaller than the previously compiled value that had been obtained by an HF calculation and an additional empirical correction factor [10]. The factor-of-2 difference found for the ^{70}Zn cross section, which had been inferred from purely theoretical HF predictions [36,38–41], reflects the uncertainty of the HF approach in this mass region.

V. ASTROPHYSICAL IMPLICATIONS

Figure 6 shows the s-process path in the region around zinc. There are two potential branchings in the reaction flow affecting the production of the important s-only nucleus ^{70}Ge. The first branching bypassing ^{70}Ge could occur between β^- decay and neutron capture at ^{69}Zn. However this branching is not open, since the β^- half-lives of ground and isomeric states are too short (1 h and 14 h). Therefore, ^{69}Zn will always undergo a β^- decay before capturing a neutron. The second potential branching could occur between β^- and electron capture (EC) decays at ^{70}Ga. However, the EC decays occurs only in 0.4% of all decays, hence the branching can be neglected. This means that the s-process path is not even partly bypassing the s-only nucleus ^{70}Ge, hence ^{70}Ge is a well suited normalization point between s abundance and solar abundance. On the other hand, the s-process path is completely bypassing ^{70}Zn, which makes it an r-only nucleus.

The s process in the zinc region was investigated using the nucleosynthesis code NETZ [42]. The information on the respective stellar scenarios, i.e., the effective time-dependent profiles for temperature, mass density, and neutron density in the considered burning zones, were adopted from Refs. [4,43]. The cross sections used are the latest recommended values from the KADoNiS database [32], which followed the compilation of Ref. [10].

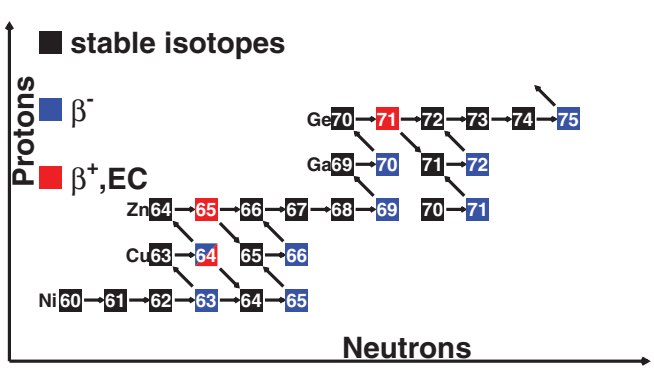

FIG. 6. (Color online) s-process reaction network in the region around Zn.

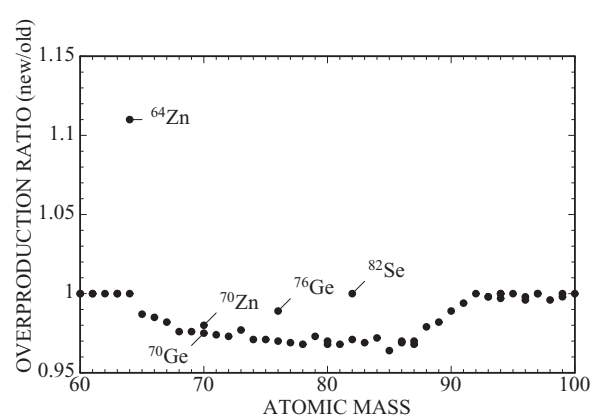

FIG. 7. The effect of the new ^{64}Zn data for the overproduction in the weak s process. ^{70}Ge is used as a normalization point of the s-process abundances. Because ^{70}Zn is bypassed during the weak s process, its strongly reduced cross section has no significant impact. This holds true also for the neutron-rich isotopes of germanium and selenium (^{76}Ge, ^{82}Se).

The most important change in the abundance distribution of the weak s process results from the new, reduced neutron-capture cross section of ^{64}Zn. The comparison of the overabundance factors in Fig. 7 shows that the abundance of ^{64}Zn is increased by 11%, while most of the heavier elements up to mass 90 are produced with slightly less abundance because of the aforementioned propagation effect, which is typical for the conditions of the weak s process. This effect reflects the fact that the local equilibrium of the s process is not reached during the conditions of the weak s-process component.

VI. SUMMARY

The neutron capture cross sections of ^{64}Zn, ^{68}Zn, and ^{70}Zn have been measured with the activation technique in a quasistellar neutron spectrum corresponding to a thermal energy of $kT = 25$ keV. Samples of natural isotopic composition were used.

By a series of repeated irradiations with different experimental conditions, the ^{64}Zn$(n,\gamma)^{65}$Zn cross section was determined to be 53.5 ± 1.5 mb, and the partial cross section ^{68}Zn$(n,\gamma)^{69}$Zn^m feeding the isomeric state in ^{69}Zn was found to be 3.30 ± 0.09 mb for the experimental spectrum. Values of 6.79 ± 0.34 mb and 4.2 ± 0.7 mb were found for the partial cross sections of ^{70}Zn$(n,\gamma)^{71}$Zn^m and ^{70}Zn$(n,\gamma)^{71}$Zn^g, which had not been measured so far.

The half-life of ^{71}Zn^m was determined to be 4.125 ± 0.007 h, with a significantly improved accuracy compared to the previous recommendation. The weighted average of the combined data yields a value of 4.120 ± 0.007 h.

Compared to previous measurements on ^{64,68}Zn, the uncertainties could also be significantly improved, while the ^{70}Zn cross section was found to be two times smaller than existing model calculations. From these results Maxwellian average cross sections were determined between 5 and 100 keV.

The consequences of these data have been studied by network calculations based on the temperature and neutron-density profiles for convective core He burning and convective shell C burning in massive stars. These simulations of the weak s process revealed that only the change of the ^{64}Zn$(n,\gamma)^{65}$Zn cross section results in significant abundance changes compared to the previous set of MACS values. The other cross sections have much smaller impact because the MACS of ^{68}Zn did not change and ^{70}Zn lies outside the main path of the weak s-process component.

ACKNOWLEDGMENTS

We would like to thank E.-P. Knaetsch, D. Roller, and W. Seith for their support at the Karlsruhe Van de Graaff accelerator. This work was supported by the HGF Young Investigators Project No. VH-NG-327 and the EuroGenesis project MASCHE.

[1] C. Travaglio, D. Galli, R. Gallino, M. Busso, F. Ferrini, and O. Straniero, Astrophys. J. **521**, 691 (1999).
[2] C. Travaglio, R. Gallino, E. Arnone, J. Cowan, F. Jordan, and C. Sneden, Astrophys. J. **601**, 864 (2004).
[3] C. Raiteri, M. Busso, R. Gallino, and G. Picchio, Astrophys. J. **371**, 665 (1991).
[4] C. Raiteri, R. Gallino, M. Busso, D. Neuberger, and F. Käppeler, Astrophys. J. **419**, 207 (1993).
[5] M. Limongi, O. Straniero, and A. Chieffi, Astrophys. J. Suppl. **129**, 625 (2000).
[6] T. Rauscher, A. Heger, R. Hoffman, and S. Woosley, Astrophys. J. **576**, 323 (2002).
[7] M. Heil, F. Käppeler, E. Uberseder, R. Gallino, and M. Pignatari, Phys. Rev. C **77**, 015808 (2008).
[8] M. Heil, F. Käppeler, E. Uberseder, R. Gallino, S. Bisterzo, and M. Pignatari, Phys. Rev. C **78**, 025802 (2008).
[9] M. Pignatari, R. Gallino, M. Heil, M. Wiescher, F. Käppeler, F. Herwig, and S. Bisterzo, Astrophys. J. **710**, 1557 (2010).
[10] Z. Bao, H. Beer, F. Käppeler, F. Voss, K. Wisshak, and T. Rauscher, At. Data Nucl. Data Tables **76**, 70 (2000).
[11] I. Dillmann, R. Plag, F. Käppeler, and T. Rauscher, in *EFNUDAT Fast Neutrons, Scientific Workshop on Neutron Measurements, Theory & Applications* (JRC-IRMM, Geel, 2009) [http://www.kadonis.org].
[12] G. Bihain, G. Israelian, R. Rebolo, P. Bonifacio, and P. Molaro, Astron. Astrophys. **423**, 777786 (2004).
[13] Y. Chen, P. Nissen, and G. Zhao, Astron. Astrophys. **425**, 697705 (2004).
[14] P. Nissen, Y. Chen, M. Asplund, and M. Pettini, Astron. Astrophys. **415**, 9931007 (2004).
[15] H. Beer and F. Käppeler, Phys. Rev. C **21**, 534 (1980).
[16] N. Patronis, S. Dababneh, P. A. Assimakopoulos, R. Gallino, M. Heil, F. Käppeler, D. Karamanis, P. E Koehler, A. Mengoni, and R. Plag, Phys. Rev. C **69**, 025803 (2004).
[17] S. O'Brien, S. Dababneh, M. Heil, F. Käppeler, R. Plag, R. Reifarth, R. Gallino, and M. Pignatari, Phys. Rev. C **68**, 035801 (2003).
[18] U. Ratzel, C. Arlandini, F. Käppeler, A. Couture, M. Wiescher, R. Reifarth, R. Gallino, A. Mengoni, and C. Travaglio, Phys. Rev. C **70**, 065803 (2004).
[19] W. Ratynski and F. Käppeler, Phys. Rev. C **37**, 595 (1988).
[20] J. de Laeter, J. Böhlke, P. de Bièvre, H. Hidaka, H. Peiser, K. Rosman, and P. Taylor, Pure Appl. Chem. **75**, 683 (2003).
[21] E. Browne and J. Tuli, Nucl. Data Sheets **111**, 2425 (2010).
[22] M. Bhat and J. Tuli, Nucl. Data Sheets **90**, 269 (2000).
[23] K. Abusaleem and B. Singh, Nucl. Data Sheets **112**, 133 (2011).
[24] X. Huang, Nucl. Data Sheets **110**, 2533 (2009).
[25] S. Dababneh, N. Patronis, P. Assimakopoulos, J. Görres, M. Heil, F. Käppeler, D. Karamanis, S. O'Brien, and R. Reifarth, Nucl. Instrum. Methods Phys. Res., Sect. A **517**, 230 (2004).
[26] V. Levkovskii, At. Energ. **4**, 79 (1958).
[27] T. Thwaites and W. Pratt, Phys. Rev. **124**, 1526 (1961).
[28] T. Sonnino, E. Eichler, and S. Amiel, Nucl. Phys. A **54**, 568 (1964).
[29] R. Reifarth, C. Arlandini, M. Heil, F. Käppeler, P. Sedyshev, M. Herman, T. Rauscher, R. Gallino, and C. Travaglio, Astrophys. J. **582**, 1251 (2003).

[30] R. Reifarth, M. Heil, F. Käppeler, and R. Plag, Nucl. Instrum. Methods Phys. Res. Sect. A **608**, 139 (2009).
[31] R. Macklin (private communication); see also Nucl. Sci. Eng. **79**, 265 (1981).
[32] I. Dillmann, M. Heil, F. Käppeler, R. Plag, T. Rauscher, and F.-K. Thielemann, in *Capture Gamma-Ray Spectroscopy and Related Topics*, edited by A. Woehr and A. Aprahamian, AIP Conf. Proc. No. 819 (AIP, New York, 2006), p. 123 [http://www.kadonis.org].
[33] J. B. Garg, V. K. Tikku, J. Halperin, and R. Macklin, Phys. Rev. C **23**, 683 (1981).
[34] J. B. Garg, V. K. Tikku, J. A. Harvey, J. Halperin, and R. L. Macklin, Phys. Rev. C **25**, 1808 (1982).
[35] M. Murty, K. Siddappa, and J. Rao, J. Phys. Soc. Jpn. **35**, 8 (1973).
[36] T. Rauscher and F.-K. Thielemann, At. Data Nucl. Data Tables **75**, 1 (2000).
[37] I. Dillmann, R. Plag, F. Käppeler, and T. Rauscher, in *International Symposium on Nuclear Astrophysics–Nuclei in the Cosmos–IX*, PoS(NIC-IX)090 [http://pos.sissa.it].
[38] M. Harris, Astrophys. Space Sci. **77**, 357 (1981).
[39] S. Woosley, W. Fowler, J. Holmes, and B. Zimmerman, At. Data Nucl. Data Tables **22**, 371 (1978).
[40] S. Goriely, Institut d'Astronomie et d'Astrophysique, Université libre de Bruxelles, report, 2002 (unpublished).
[41] S. Goriely, Institut d'Astronomie et d'Astrophysique, Université libre de Bruxelles, report, 2005 (unpublished).
[42] S. Jaag, Forschungszentrum Karlsruhe, report, 1991 (unpublished).
[43] C. Raiteri, M. Busso, R. Gallino, G. Picchio, and L. Pulone, Astrophys. J. **367**, 228 (1991).